Chemical Engineering Journal 521 (2025) 166932

Contents lists available at ScienceDirect

Chemical Engineering Journal

journal homepage: www.elsevier.com/locate/cej

Modulating the local electron distribution of *reo*-NH_2-UiO-66 through Fc-CHO functionalization for the effective photodegradation of single and mixed VOCs

Jiajun Yu [a,1], Xiao Wang [a,*,1], Shijie Yang [a,b], Xiaofeng Xie [a], Jing Sun [a,*]

[a] State Key Lab of High Performance Ceramics and Superfine Microstructure, Shanghai Institute of Ceramics, Chinese Academy of Sciences, 585 Heshuo Road, Shanghai 201899, China
[b] University of Chinese Academy of Sciences, 19 (A) Yuquan Road, Beijing 100049, China

ARTICLE INFO

Keywords:
reo-NH_2-UiO-66
Fc-CHO
Ligand functionalization
Photocatalysis
VOCs

ABSTRACT

Ligand functionalization could effectively modulate the local electron distribution of MOFs, thus improving their performance in both the capturing and photocatalytic oxidization of various VOCs. In this work, a series of Fc-CHO/NU-X (X = 1, 2, 3, 4) were obtained through the ligand functionalization of *reo*-NH_2-UiO-66 (denoted as NU) with ferrocenecarboxaldehyde (Fc-CHO) as the modifier. By altering the local charge distribution and inducing Fe-OH and cyclopentadienyl rings as new adsorption sites, Fc-CHO altered the adsorption behavior of both aromatic and oxygenated VOCs and consequently their degradation pathways. The introduction of electron-donating Fc-CHO enhanced the ligand to metal charge transfer (LMCT), accelerated the electron-hole separation and therefore promoted the effective formation of oxidative radicals, facilitating the effective oxidation of acetaldehyde. Direct charge transfer through p-p interaction enabled the ring-opening and deep oxidation of toluene. The degradation efficiencies of toluene and acetaldehyde increased from 25 % and 28 % (NU) to 80 % (Fc-CHO/NU-3) and 65 % (Fc-CHO/NU-2), respectively. Positive effects of Fc-CHO functionalization were also observed during the removal of acetaldehyde-toluene mixtures and the synergistic effect between acetaldehyde and toluene was revealed. This work provides new ideas and novel materials for the purification of in-door air pollutants.

1. Introduction

Volatile organic compounds (VOCs), which include aromatic hydrocarbons, oxygenated VOCs (OVOCs), olefins, alkynes, and so on, have drawn much attention in recent years given their roles as precursors of PM2.5 and ozone, along with their irritating and carcinogenic effects to human body. The development of VOCs purification methods which are both eco-friendly and energy-saving is essential for creating high quality living environments. Photocatalysis, which directly utilizes sunlight energy to generate photogenerated electron-hole pairs and catalyze redox reactions, has emerged as an effective means in purifying low concentration VOCs considering its advantages like low-cost, energy-saving and eco-safety.

Metal-organic frameworks (MOFs), formed by the coordination between metal ions/clusters and organic ligands, are among the most promising catalysts for gaseous reactions due to their large specific surface area, permanent porous structure and adjustable chemical properties [1,2]. Despite the tremendous number of active sites, the application of MOFs as photocatalysts is still limited due to their poor charge transfer ability, which shortens the lifetime of excited electron-hole pairs and hinders the generation of oxidative radicals. Besides, most research work today only concentrate on a single type of VOCs, ignoring the co-existence of multiple VOCs in practical environment. Revealing the synergistic or competitive mechanism during the adsorption/degradation of mixed VOCs, is also crucial for the practical application of MOFs.

In the purpose of accelerating the transfer of photo-excited electrons in MOFs, several means have been developed [3]. The implantation of co-catalysts with high conductivity, including metal nanoparticles (or metal clusters) [4,5], carbon nanostructures [6], polyoxometalates [7,8]

* Corresponding authors.
E-mail addresses: wangxiao@mail.sic.ac.cn (X. Wang), jingsun@mail.sic.ac.cn (J. Sun).
[1] These authors contribute equally to this article.

https://doi.org/10.1016/j.cej.2025.166932
Received 19 May 2025; Received in revised form 25 July 2025; Accepted 6 August 2025
Available online 7 August 2025

and semiconductors [9,10], is among the most promising methods. However, despite their ability in modulating the electron transfer paths in MOFs, these co-catalysts sometimes block the pores of MOFs and therefore hinder the migration and adsorption of VOCs. In addition, the lack of bonds between MOFs and co-catalysts also limits the charge transfer between them.

Ligand functionalization has also been found as an effective way in optimizing the performance of MOFs [11–14]. By Cl functionalization, Yang et al. [15] optimized the performance of MFM-68 and UiO-66 in capturing trace benzene. −CH···Cl and Cl···π interactions were found to play a key role in the adsorption of benzene. In addition to providing active sites, ligand functionalization could also improve the photocatalytic performance of MOFs by altering the distribution of electrons or forming new pathways for charge transfer [16]. Li et al. [17] found that by changing the substituent groups of UiO-66 from -NH_2 to -NO_2, its optical bandgap could be adjusted by 1 eV. The different electron-donating and electron-accepting effects of the two substituents influenced the electron density of ligand in UiO-66, which was found as the main reason for the change of the highest occupied molecular orbital (HOMO) level in MOFs. However, most functionalization methods can only introduce one unique feature and may even cause adverse effects such as pore blocking or weakened active sites, which cannot satisfy the rapid capture and efficient degradation of VOCs at the same time. How to simultaneously optimize both the adsorption active sites and photoelectric conversion properties of MOFs, is still a research gap to be filled.

The ferrocene (Fc) family, which comprises ferrocenecarboxylic acid (Fc-COOH), ferrocenecarboxaldehyde (Fc-CHO), and other derivatives with varying substituents, is a classic organometallic complex [18] characterized by two cyclopentadienyl rings coordinated to a central iron atom. Thanks to the outstanding charge transport properties [19] of Fc compounds, their applications span diverse fields, including chemodynamic therapy [20], electrocatalysis (hydrogen and oxygen evolution) [21,22], and photocatalysis [10,19,23]. Xia et al. composite ferrocene with NH_2-UiO-66 via the coordination between Fc-COOH and open Zr sites to promote the separation and transfer of charge carriers. Fc itself can act as photosensitizer and generate high-energy photoelectrons under light illumination. The combined effects efficiently promote the photoreduction of CO_2 [24,25]. In addition to functioning as conductive co-catalysts, ferrocene (Fc) can also generate additional adsorption sites for aromatic compounds via π-conjugation between its cyclopentadiene (Cp) ring and aromatic VOCs [26,27].

As discussed above, the combination of Fc with MOFs through ligand functionalization could provide us with an effective path to optimize the electron migration ability while maintaining or improving the adsorption capacity of MOFs, so as to obtain efficient bifunctional materials for the adsorption and photocatalytic degradation of VOCs. The application of Fc functionalized MOFs (Fc-MOFs) in VOCs purification has not been thoroughly studied and the interaction mechanism between Fc-MOFs and VOCs guests is unclear. Herein, by using Fc-CHO as the modifier, ligand functionalization is conducted on *reo*-NH_2-UiO-66 (denoted as NU) to synthesize Fc-CHO functionalized NU composites (denoted as Fc-CHO/NU) through the post-synthetic Schiff-base reaction between -CHO and -NH_2. Toluene and acetaldehyde are selected as representatives of aromatic and OVOCs pollutants to test the performance of Fc-CHO/NU. The introduction of Fe sites and cyclopentadienyl rings, as active sites, significantly improve the adsorption capacity of VOCs. The electron-donating and photosensitizer effects of Fc-CHO effectively optimize the photo-electric performance of NU and promote the generation of both •OH and $\bullet O_2^-$ radicals. Compared to pristine NU, the Fc-CHO/NU samples exhibit nearly a 2-fold increase in the capture capacity of VOCs, along with 2.3- and 3.2-folds enhancements in the catalytic degradation efficiency of acetaldehyde and toluene, respectively, which provides a novel idea for the design and performance optimization of MOFs photocatalysts for VOCs purification. In addition, to mimic practical environment, the adsorption and photocatalytic removal of mixed pollutants have also been tested and synergistic degradation effects have been revealed, providing experimental basis for the practical application of novel MOFs photocatalysts in indoor air purification.

2. Experimental section

2.1. Materials

Zirconium tetrachloride ($ZrCl_4$, ≥ 99.9 %) and ethyl alcohol (EtOH, C_2H_6O, ≥ 99.7 %) were purchased from Shanghai Aladdin Biochemical Technology Co., Ltd. *N*, *N*-dimethylformamide (DMF, C_3H_7NO, 99.5 %), 2-aminoterephthalic acid (H_2BDC-NH_2, $C_8H_7NO_4$, 99.0 %) and ferrocenecarboxaldehyde (Fc-CHO, $C_{11}H_{10}FeO$, 98 %) were purchased from Shanghai Adamas Reagent Company.

2.2. Samples preparation

2.2.1. Synthesis of *reo*-NH_2-UiO-66

The *reo*-NH_2-UiO-66 was prepared according to our previous study [28]. 0.35 g $ZrCl_4$, 0.27 g H_2BDC-NH_2, and 0.5 mL deionized water were added to 50 mL DMF and stirred for 1 h. The solution was placed into a 100 mL high-pressure reactor and held at 120 °C for 24 h. The product was washed three times with DMF and ethanol (EtOH), respectively, and dried under vacuum at 100 °C for 8 h to obtain *reo*-NH_2-UiO-66 (denoted as NU).

2.2.2. Synthesis of Fc-CHO/NU

0.5 g NU was dissolved in 50 mL of DMF and sonicated for 30 min. X mmol (X = 0, 0.5, 1.5, 3.0, 4.5) of Fc-CHO was added to the above suspension and sonicated for 30 min. The mixed suspension was transferred into an autoclave reactor and held at 120 °C for 24 h, and then cooled to room temperature. The precipitates were washed with DMF and EtOH, respectively, and then dried under vacuum at 100 °C for 8 h. The samples obtained were named as NU (X = 0), Fc-CHO/NU-1 (X = 0.5), Fc-CHO/NU-2 (X = 1.5), Fc-CHO/NU-3 (X = 3.0), Fc-CHO/NU-4 (X = 4.5).

2.3. Characterization

XRD patterns were collected by a Rigaku D/max 2550 *V* X-ray Powder diffractometer. The distribution and weight ratio of elements in the samples was observed by scanning electron microscope (SEM, FEI Magellan 400) equipped with an energy dispersive spectroscopy (EDS) energy spectrometer and Inductively Coupled Plasma Optical Emission Spectrometer (ICP-OES, Agilent). X-ray photoelectron spectroscopy (XPS) results were obtained through a Thermo Fisher ESCALAB 250 X-ray Photoelectron Spectroscopy. The light adsorption spectra (UV/vis) were collected by a Perkin Elmer Lambda 1050 UV/vis spectrophotometer. Photoluminescence (PL) spectra were obtained through a Perkin Elmer LS55 fluorescence spectrometer. The photocurrent curves of the samples were measured by a photovoltage spectrometer (CEL-SPS1000, Zhongjiaojinyuan, Beijing, China). Temperature Programmed Desorption (TPD) analysis was conducted on the Bibuilder ChemiSorb PCA-1200 instrument.

2.3.1. Adsorption of acetaldehyde and toluene

Breakthrough experiments were conducted to investigate the adsorption behavior of low-concentration VOCs. Specifically, 35 mg of photocatalyst powder (either NU or Fc-CHO/NU) was loaded into a fixed-bed reactor. A gaseous mixture of toluene (23.5 ppm) or acetaldehyde (50 ppm), using N_2 as the carrier gas, passed through the samples at constant flow rates of 170 mL/min and 160 mL/min, respectively. The outlet gas was continuously monitored by GC-FID to track the target VOC concentrations until adsorption saturation was reached. The dynamic adsorption capacities (***A***) of the catalysts were then calculated using **Eq. (1)**.

$$A = \frac{C_0 * v * \left[\int_0^T \frac{\left(C_{blank,t} - C_t\right)}{C_0} dt\right]}{22.4} * M * 10^{-6} * \left(\frac{1}{m}\right) \quad (1)$$

In Eq. (1), C_0 represents initial and real-time concentrations of target VOCs. $C_{blank,t}$ and C_t stand for the real-time concentrations of VOCs without and with the implantation of adsorbents, respectively. M represents the molar mass of target VOCs while m is the weight of adsorbents applied (35 mg) in our experiments. T is the time needed to reach adsorption saturation and *v* is the flow rate of inlet gases.

2.3.2. Photocatalytic performance measurements

The photocatalytic experiments were carried out in a domestic reaction system as shown in Scheme S1. A glass plate (150 mm × 75 mm) coated with 50 mg of catalyst was placed into the reaction chamber. Toluene (10 ppm), acetaldehyde (200 ppm) or acetaldehyde-toluene mixtures (10 ppm for toluene and 200 ppm for acetaldehyde) diluted with air continuously passed over the catalyst surface at a flowrate of 20 mL/min throughout the experiments. Adsorption was firstly performed in the dark. After reaching the adsorption-desorption equilibrium, a xenon lamp (500 W, 30 cm above the catalyst) was turned on. The concentrations of toluene and acetaldehyde were detected by gas chromatography every 10 min. During the photocatalytic experiments, a humidifier tank and a water-cooling system were applied to keep the chamber at a steady relative humidity of 55–60 % RH and a temperature of ~25 °C. The humidifier tank was removed from the reaction system in the water-free experiments to obtain a relative humidity of ~5 % RH. The photocatalytic experiments were repeated for 3 times to ensure reproducibility and clarity.

Cyclic degradation reactions were conducted under the same conditions as photocatalytic reactions. After each cycle, the photocatalyst was irradiated by 500 W Xenon light in air flow for 2 h to remove the accumulated intermediates and recover photocatalytic activity.

2.3.3. Mechanism investigation

The mineralization ratio was studied to reveal the photocatalytic degradation mechanisms. In the purpose of eliminating the influence of CO_2 in air, a N_2/O_2 (80:20) mixture was applied as the carrier gas. The concentration of CO_2 in the outlet gas was monitored through GC-TCD. The curves CO_2 concentrations measured during the reaction processes were integrated to calculate the real-time and total VOC mineralization ratio (Eq. (2)).

$$MR = \frac{\left(\int_0^T C_{t1} dt\right) * v}{\int_0^T \left(C_{0\ voc} - C_{t\ voc}\right) dt * v * n} \quad (2)$$

In Eq. (2), MR represents the total mineralization ratio of target VOCs, C_{t1} is the concentration of CO_2 detected during the photocatalytic reactions. $C_{0\ VOC}$ and $C_{t\ VOC}$ stand for the initial and real-time concentrations of target VOCs, respectively. n is the number of carbon atoms in the VOC molecules (7 for toluene and 2 for acetaldehyde) and *v* is the flow rate of inlet gases (20 sccm). T is the total time of reaction.

In addition to the mineralization ratio, intermediates formed during the degradation of toluene and acetaldehyde are also characterized through in-situ FTIR (Fourier Transform infrared spectroscopy) analysis and PTR-ToF-MS (Proton transfer reaction- Time of flight- Mass spectroscopy). In-situ FTIR is carried out on an IRTracer-100 Fourier Transform Infrared Spectrophotometer equipped with a Harrick Praying Mantis reaction chamber. Photocatalyst was loaded in the chamber. VOCs with the same concentration and flowrates as the photocatalytic degradation reactions continuously passed the chamber during the whole reaction processes. FTIR spectra are collected every 30 min. PTR-ToF-MS spectra is collected on a IONICON PTR-TOF 6000 X2 mass spectrometer. Specifically, outlet gas of the photocatalytic reactions is collected by aluminum foil gas bags after reaching the adsorption equilibrium and 1 h after starting the photocatalytic reactions. Every collection lasts for 10 min. N_2 flow with constant flowrate is applied to dilute the outlet gas to meet the detection limit of PTR-ToF-MS. MS spectroscopy are obtained by using H_3O^+ as the proton source.

3. Results and discussion

3.1. Synthesis and Characterization of Fc-CHO/NU

After the post-synthetic treatment of *reo*-NH_2-UiO-66 with Fc-CHO, a series of Fc-CHO/NU samples were obtained [29]. The micromorphology and the elements distribution are firstly analyzed to find the impacts of Fc-CHO on NU. As given by the SEM images (Fig. 1 a-c), the NU sample is mainly composed of nanocubes with an average size of ~120 nm. The dosage of Fc-CHO does not significantly change the particle size and morphology of the samples. Zr, Fe, C, and O are uniformly distributed in the Fc-CHO samples (Fig. 1 d-i) and the weight percentage of Fe increases proportionally with the dosage of Fc-CHO (Table S1), confirming the successive implantation of Fc-CHO.

Elucidating the interactions between NU substrate and the Fc-CHO guests is the basis for understanding the synthesis mechanism and the properties of Fc-CHO/NU. As given by the XRD patterns (Fig. 2a), in addition to the diffraction peaks of UiO-66, broad diffraction peaks at 4° and 6° are observed, indicating the formation of cluster defects with short-range ordering, a unique feature of *reo* topology [30,31]. The position of diffraction peaks of Fc-CHO/NU samples are similar to those of NU, indicating that the introduction of Fc-CHO does not interfere with the lattice structure of MOFs. The diffraction peaks corresponding to *reo* defects gradually disappear, which might be due to the grafting of Fc-CHO to the defect sites [19]. FTIR spectra of Fc-CHO/NU samples are collected. The characteristic peak for the vibration of the metallocene skeleton in Fc-CHO (1097 cm^{-1}) appears, together with a red-shift of the asymmetric vibration of N—H bonds (3364 cm^{-1}), suggesting the presence of conjugation effects or hydrogen bonding between NU and Fc-CHO molecules. An intensity increase is found in the peak at 1653 cm^{-1}, confirming the formation of -C=N- bonds through the Shiff-base reaction between -CHO and -NH_2 groups [29]. The strong -C=N- covalent bonds between Fc-CHO and NU not only prevent the aggregation and leaching of Fc-CHO [32], but also provide new bridges for charge transfer. As confirmed by the XPS results (Fig. 2d), unlike the circumstance of pure Fc-CHO, in which Fe(II) is found as the predominant state of Fe, an obvious increase in the proportion of Fe(III) happens in the Fc-CHO/NU sample, confirming the loss of electrons [33]. Meanwhile, the Zr 3d peak red-shifts (Fig. 2e), indicating an increase in the electron density of Zr nodes [19]. As a molecule with high electron density, Fc-CHO tends to donate electrons to the Zr nodes through the -C=N- bonds, leading to the formation of Fe(III). The coordination environment of N atoms in -NH_2 of the organic ligand aminoterephthalic acid in NU was also analyzed (Fig. S1). The peak of N blue-shifts after the introduction of Fc-CHO. This is because the sandwich-like ferrocene with an off-domain electronic structure increases the conductivity of the MOFs and accelerates the transfer of electrons from the ligand to the Zr center [34,35], causing a decrease in the electron density of -NH_2 groups. The acceptance of electrons by Zr weakens the strength of Zr—O bonds, resulting in a slight decrease in the weight loss temperature from ~350 °C of NU to ~300 °C of Fc-CHO/NU samples as observed in Fig. S2. As the photocatalytic degradation of VOCs happens at room temperature, the slight decrease in the thermal stability of the samples shows almost no negative effects on the performance of Fc-CHO/NU photocatalysts.

The textual structure, which usually includes the specific surface area and pore structure of MOFs, is also characterized. As shown by Fig. 2 f, all samples exhibit type IV adsorption-desorption isotherms, suggesting the presence of both micro- and mesopores (Fig. 2f and Fig. S3). Two kinds of micropores, with sizes centered at 0.6 nm and 1.1 nm, were found, which could be assigned to *fcu* NH_2-UiO-66 and *reo* defects, respectively. The number of 1.1 nm pores decreased

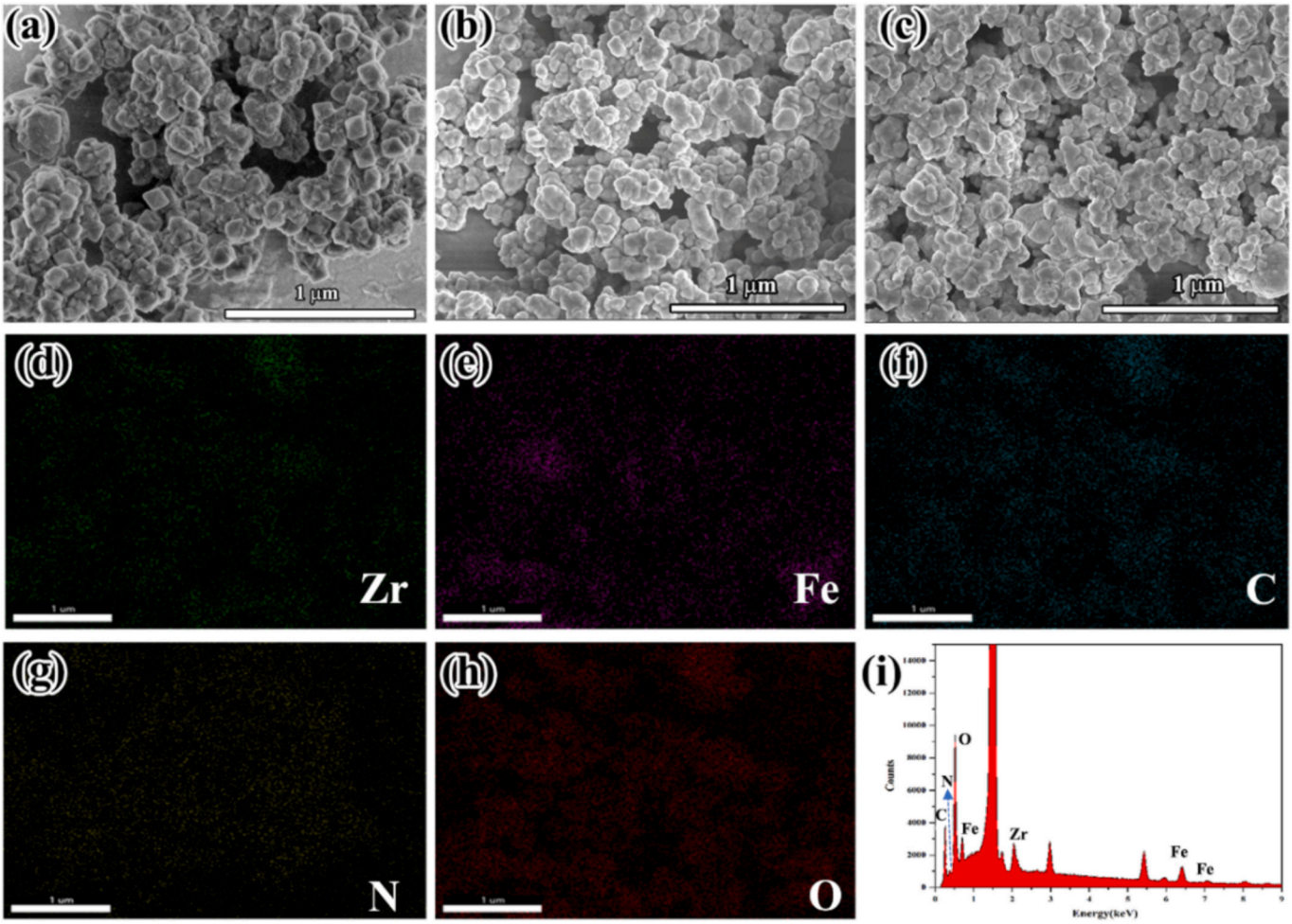

Fig. 1. The SEM images of (a) NU, (b) Fc-CHO/NU-2 and (c) Fc-CHO/NU-3 (Magnification: 50 k X, Extra high tension: 1 kV); (d-h) the EDS-mapping analysis of Zr, Fe, C, N, O elements of Fc-CHO/NU-3 and (i) the corresponding EDS spectra.

continuously with the addition of Fc-CHO, probably because Fc-CHO preferentially connects to the defect sites and occupies these pores, which leads to a slight diminution in the specific area from 733 m^2/g of NU to 640 m^2/g of Fc-CHO/NU-3 (Table S2). However, with the dosage of excess Fc-CHO (Fc-CHO/NU-4), the number of both 0.6 nm and 1.1 nm pores decreases, together with a reduction in the specific surface area (495 m^2/g), demonstrating that Fc-CHO starts to occupy the pores of *fcu*-NH_2-UiO-66.

Based on the analysis results, the implantation mechanism of Fc-CHO on NU could be proposed. During the secondary solvothermal process, Fc-CHO firstly enters the 1.1 nm pores of NU and connects with exposed -NH_2 through the Schiff-base reaction between -CHO and -NH_2. When further increasing the concentration of Fc-CHO, it starts to enter the 0.6 nm pores and grafts on the ligands. The covalent -C=N- bonds between Fc groups and NU substrate prevent the Fc groups from leaching and enable the migration of electrons from Fc to Zr nodes. As active sites, the change of electron density of Zr node would not only influence the adsorption behavior of VOCs, but also interfere with the photo-excited ligand-to-metal charge transfer (LMCT) in NU [36,37], therefore affecting their photocatalytic properties.

3.2. Photoelectric conversion performance of Fc-CHO/NU

The light absorption ability, as well as the excitation and migration of charge carriers, are key factors affecting the photoelectric conversion efficiencies of MOFs. As shown in Fig. 3a, the introduction of Fc-CHO effectively promotes the absorption of both UV and visible light, and causes red-shifts in the absorption edges. As an effective electron-donor, Fc group would contribute electrons to NH_2-BDC linkers and alter the position of HOMO of NU, which broadens the light absorption range and makes it easier for the excitation of electrons. As a photosensitizer, Fc would absorb light and generate excited electrons. Both of the above effects contribute to the improved light absorption ability of Fc-CHO/NU samples. PL intensity, which reflects the electron-hole recombination ratio, is another key indicator for evaluating the photoelectric conversion ability of catalysts. Compared with NU, Fc-CHO/NU-2 and Fc-CHO/NU-3 samples exhibit much lower PL intensity (Fig. 3b). Fc-CHO, with an off-domain electronic structure, improves the conductivity of NU and promoted the migration of excited electron and holes, both inhibit the recombination of charge carriers. Similar results could be observed in the transient fluorescence spectra (Fig. 3d). Due to the easy recombination of electron-hole pairs, NU is dominated by short-lifetime (0.30 ns) carriers, which accounted for 82 % of the total (Table S3). After the introduction of Fc-CHO, the proportion of short- lifetime carriers in the Fc-CHO/NU-1 to Fc-CHO/NU-3 samples gradually declined from 85 % to 31 %, and the lifetime was shortened from 0.26 ns to 0.16 ns. The proportion of long- lifetime carriers gradually increased from 15 % to 69 %, and the lifetime was extended from 2.25 ns to 2.91 ns, further confirming the effectiveness of Fc-functionalization in preventing charge recombination. As a result of the improved light absorption ability and the promoted separation of electron-hole pairs, significantly higher photocurrent densities in Fc-CHO/NU-2 and -3 (Fig. 3c) than pristine NU are found, reflecting an increase in the concentration of excited charge carriers on the surface of photocatalysts. The decrease in the

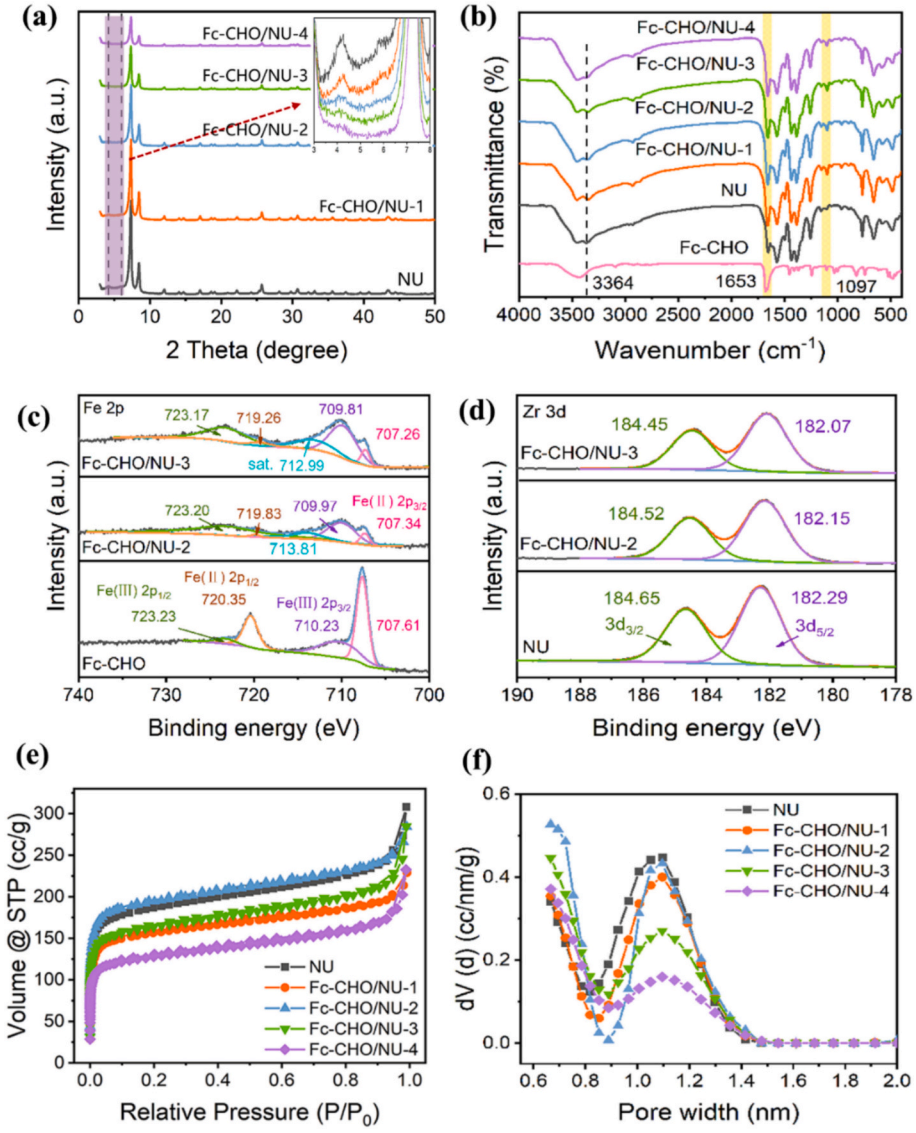

Fig. 2. (a) XRD patterns of Fc-CHO/NU samples; (b) the FTIR spectra of pure Fc-CHO and Fc-CHO/NU samples; the XPS analysis of different samples for (c) Fe 2p and (d) Zr 3d; (e) the N_2 adsorption-desorption isotherms of Fc-CHO/NU samples and (g) the distribution of micropores.

photocurrent intensity of Fc-CHO/NU-4 might be due to the fact that too much Fc-CHO did not coordinate well with the Zr sites and did not establish a good charge-transfer pathway, but rather acted as carrier recombination center. The above results confirm that the introduction of Fc-CHO modulate the charge transport pathway in the samples, realized the effective separation of electron-hole pairs and promoting their migration to the surface of photocatalysts. These charge carriers could combine with the adsorbed water and O_2 to generate oxidative radicals, which are key oxidative species for the catalytic degradation of VOCs.

The generation of superoxide radicals $\bullet O_2^-$ (Fig. 4a) and hydroxyl radicals •OH (Fig. 4b) was then characterized. Thanks to the effective excitation and migration of electrons, Fc-CHO/NU-1 and 2 showed the highest signal of $\bullet O_2^-$. Despite the high photocurrent density of Fc-CHO/NU-3, its ability in generating $\bullet O_2^-$ was slightly lower other samples, which might be attributed to its slightly lower affinity towards O_2 (Fig. S4). As the dosage of Fc-CHO further increased, they started to occupy the small pores of NU, which inhibit the migration of O_2 and limited the generation of $\bullet O_2^-$. Almost no •OH was detected in NU and Fc-CHO/NU-1, which could be attributed to the fact that the energy of holes in NU (with the HOMO located at ~2.03 eV) is not sufficient for the oxidation of H_2O into •OH (•OH/H_2O 2.27 eV). With the addition of Fc-CHO, the amount of •OH significantly increased and reached its highest in Fc-CHO/NU-3. As discussed above, the electron migration between NU and Fc-CHO generated Fe (III). The reversible conversion between Fe (III) and Fe (II) under light irradiation might be the main reason for the formation of •OH [10]. The above discussion revealed that the introduction of Fc-CHO not only facilitated carrier separation, but also induced new mechanisms for charge transfer and radical generation, which would favor the catalytic degradation of VOCs.

3.3. Adsorption of VOCs by Fc-CHO/NU photocatalysts

Adsorption, which includes the enrichment of gas molecules and their migration inside the pores of MOFs to reach catalytic active sites, is the prerequisite for the catalytic degradation of flowing VOCs. In order to investigate the performance of NU and Fc-CHO/NU catalysts in capturing VOCs with different functional groups and molecular polarity, breakthrough curves are tested and the corresponding adsorption capacity of NU and Fc-CHO/NU samples were calculated. As shown by Fig. 5, the implantation of Fc-groups significantly promotes the adsorption of VOCs. For acetaldehyde (Fig. 5a and b), the saturated adsorption capacity increases from 42.90 mg/g of NU to 77.99 mg/g of

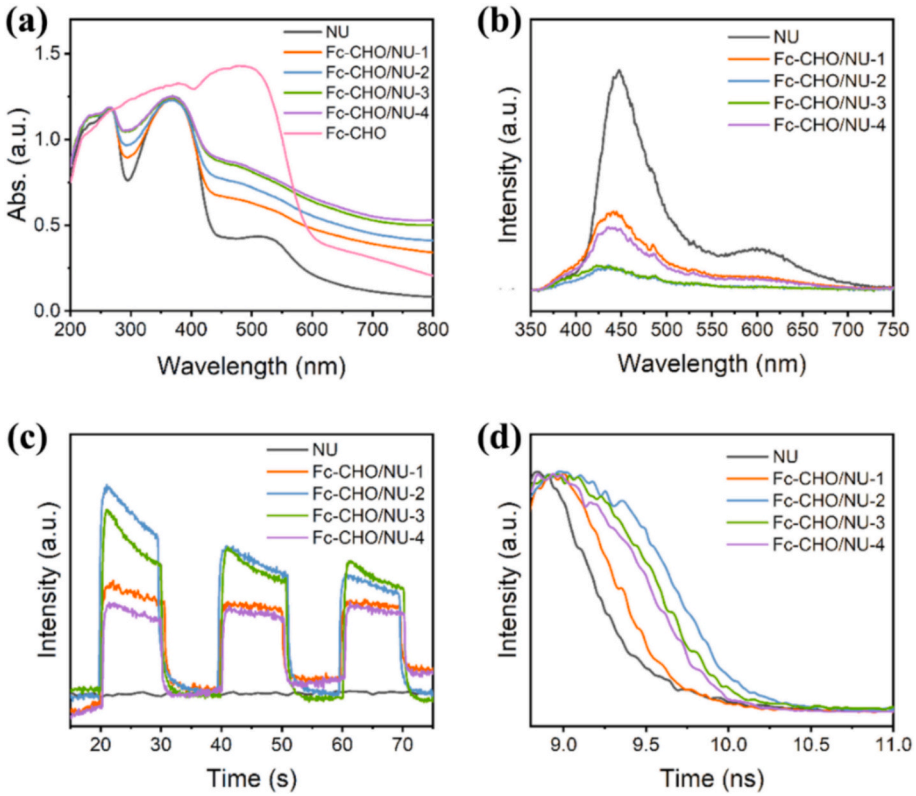

Fig. 3. (a) UV–visible absorption spectra, (b) PL spectra, (c) photocurrent response curves under xenon lamp, and (d) transient fluorescence spectra of different samples.

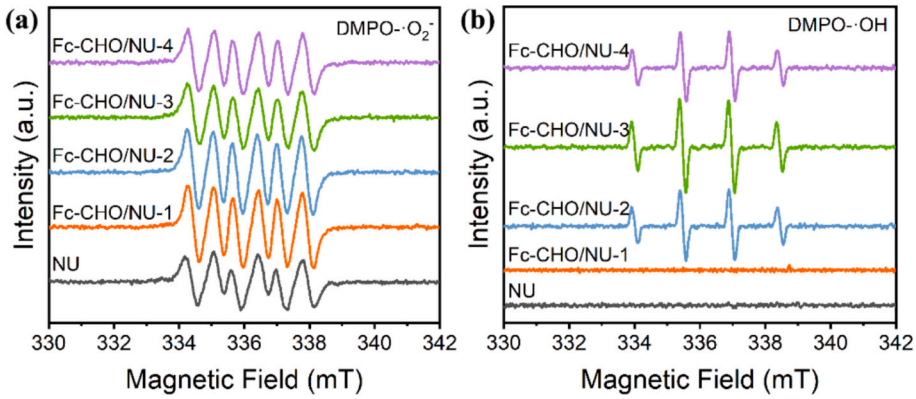

Fig. 4. The (a) ESR-•O_2^-, and (b) ESR-•OH spectra of different samples.

Fc-CHO/NU-2 and the breakthrough time increases from ~570 min/g to nearly 2000 min/g, making Fc-CHO/NU great candidates for the capture of acetaldehyde molecules. The adsorption of toluene also increases with the grafting of Fc groups (Fig. 5b and e). The highest saturated adsorption capacities for toluene are observed for Fc-CHO/NU-2 (214.59 mg/g) and – 3 (212.61 mg/g), almost twice the value of NU (109.59 mg/g) and is higher than most commonly studied adsorbents including MOFs, zeolites and activated carbon (Table S4). According to the adsorption capacity and the volume of the photocatalyst, the ability of Fc-CHO/NU samples in enriching VOCs could be roughly estimated (Eq. S1). When applying Fc-CHO/NU-2 and 3 as the photocatalyst, the concentration of acetaldehyde and toluene around the photocatalysts increase from 50 ppm (~2.23 mmol/L) and 23.5 ppm (~1.05 mmol/L) to about 274 mmol/L and 354 mmol/L, respectively, confirming its superior performance in enriching VOCs and facilitating the following photocatalytic reactions.

The adsorption behavior of gas molecules could be affected by a number of factors, including structural parameters like the specific surface area, pore structure of the samples, and open sites such as the Lewis acid/basic sites in the samples [7,38,39]. To reveal the mechanism of the changes in adsorption capacity, Lewis acid/basic sites were firstly analyzed through TPD tests. As given by Fig. 5c, NU displayed a broad desorption peak of CO_2 centered at ~230 °C, including the adsorption of CO_2 by Zr-OH and -NH_2. With the dosage of Fc-CHO, the desorption peaks obviously increased and slightly move to ~200 °C. As discussed above, the grafting of Fc groups alters the electron density of Zr nodes, adjusts the Lewis basicity of Zr-OH sites and results in the shift of desorption peak [19,40,41]. In addition, Fe-OH comes with Fc groups would also work as new Lewis basic sites. These new sites make up for the loss of -NH_2 sites caused by the Schiff-base reaction and result in the

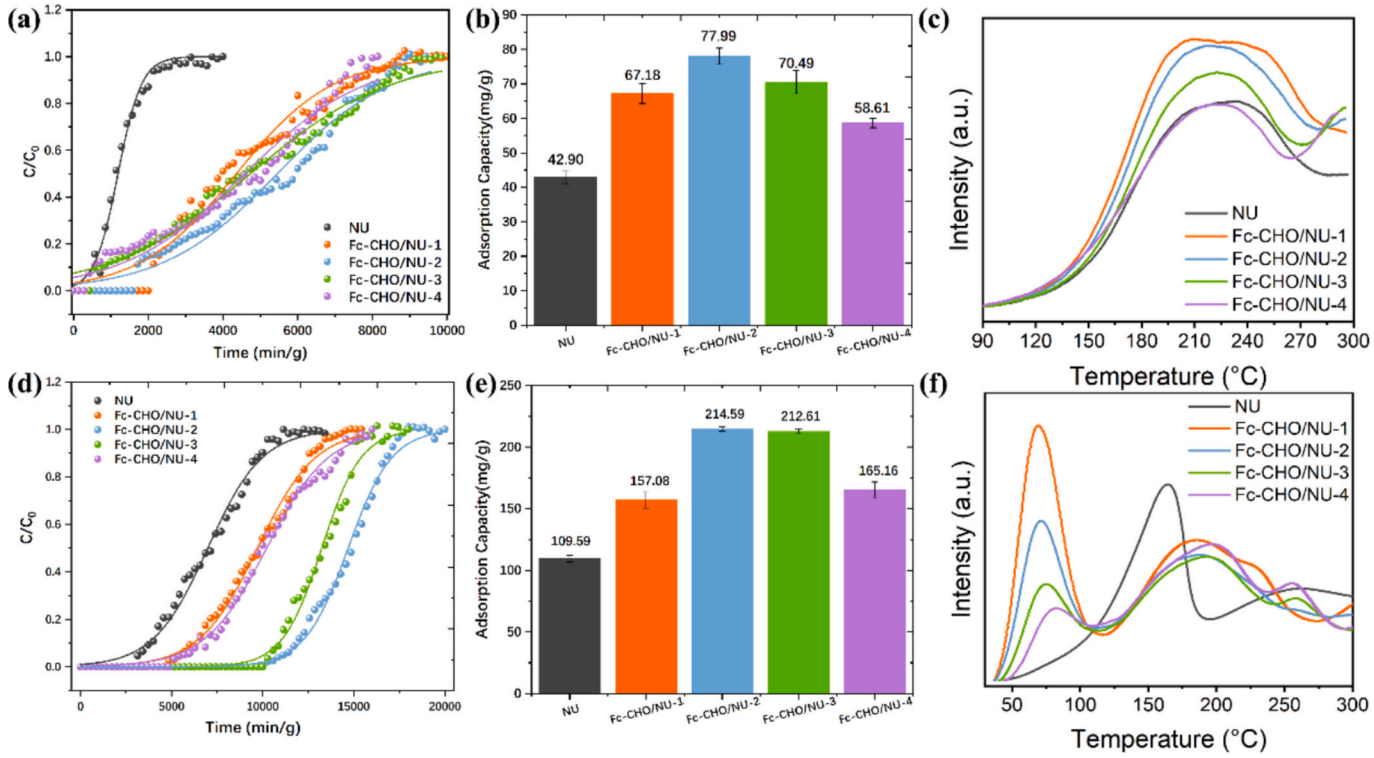

Fig. 5. (a) The acetaldehyde breakthrough curves and (b) corresponding adsorption capacities at 298 K of NU and Fc-CHO/NU samples; (c) CO_2-TPD results of NU and Fc-CHO/NU samples; (d) The toluene breakthrough curves and (d) corresponding adsorption capacities of at 298 K of NU and Fc-CHO/NU samples; (b) NH_3-TPD results of NU and Fc-CHO/NU samples.

increase in the adsorption capacity for acetaldehyde as observed in Fig. 5d and e. NH_3-TPD results reflect the changes in Lewis acid sites, which are among the predominant sites for toluene adsorption. The NH_3-TPD result of NU mainly contains two desorption peaks at 150–170 °C and 225-275 °C, reflecting two kinds of Lewis acid sites with different strengths and densities. Fc-CHO/NU samples show a new strong desorption peak at 60-80 °C. Considering the relatively lower porosity and smaller specific surface area of Fc-CHO/NU than NU, π-π stacking provided by the electron rich Cp rings of Fc groups is considered as the main reason for the new peak and the increased adsorption capacity for toluene [42].

The changes in the adsorption behavior are also confirmed through in-situ FTIR analysis (Fig. 6 and Fig. S5). Aldehydes groups are observed during the adsorption of acetaldehyde by NU and Fc-CHO/NU-2. When applying Fc-CHO/NU-2 as the photocatalyst, the shape of peaks assigned to the adsorption on -NH_2 and -OH groups vary compared to that of NU. The Schiff-base reaction between Fc-CHO and NU consumes -NH_2 groups but induces Fe-OH sites, which act as new adsorption sites for capturing acetaldehyde.

Partial oxidation happens during the adsorption of toluene by NU. When interacting with open Zr-OH sites, oxidation would happen preferentially on the substituent -CH_3 groups, leading to the formation of aldehyde groups and resulting in the FTIR peak of aldehyde groups (1716 cm^{-1}). Compared with NU, the intensity and wavenumber of peaks for benzene ring changes on Fc-CHO/NU-3, which might be related to the different adsorption behavior. In addition to the formation of benzaldehyde, the typical peak for -CH_3 (1473 cm^{-1}) is also found with Fc-CHO/NU-3 acting as the adsorbents, indicating that aside from interaction with open Zr-OH sites, π-π interaction would also happen during the adsorption of toluene, which preserves the -CH_3 groups in toluene. The peaks of υ (N—H) in -NH_2 groups appear during the adsorption and photocatalytic degradation of toluene. However, almost no difference is observed with the adsorption of degradation proceed, indicating that -NH_2 is not among the key active sites for the capturing and oxidation of toluene.

3.4. Photocatalytic degradation of VOCs and mechanism study

After characterizing the samples for their photoelectric properties and ability in capturing different VOCs, their performance as photocatalysts were tested. Fig. 7a presents the degradation curves of toluene by different samples, and the degradation efficiency of pristine NU is about 25 %. After the addition of Fc-CHO, the degradation efficiencies increases and Fc-CHO/NU-3 shows the best degradation performance (Fig. 7b). The degradation of acetaldehyde is also promoted and the efficiency increases from 28 % of NU to 65 % of Fc-CHO/NU-2 (Fig. 7d). The increased adsorption capacity, as well as the effective generation of oxidative radicals, accounts for the improved degradation efficiency. Pseudo-first-order fitting for the photocatalytic degradation of both toluene and acetaldehyde are conducted. As given by Fig. S10, Fc-CHO/NU-2 exhibits the highest K_{obs} value of 0.00914 min^{-1} during the photocatalytic degradation of acetaldehyde, while Fc-CHO/NU-3 shows the highest K_{obs} value of 0.0192 min^{-1}, 3.56 times the value of pristine NU (0.0054 min^{-1}) in the photocatalytic degradation of toluene. Although sacrificing the microporous of NU to some extent, Fc-CHO still accelerates the photocatalytic degradation of VOCs, which could be attributed to the following aspects: (1) the introduction of Fe-OH and Cp rings in Fc-CHO, as new adsorption sites for acetaldehyde and toluene, accelerates their degradation by increasing the amount of target molecules adsorbed; (2) the direct charge transfer between Cp rings and toluene through π-π stacking lowers the energy barrier for the ring-opening of toluene and promotes its photocatalytic oxidation; (3) Fc-CHO functionalization enables the generation of more oxidative radicals, which further improves the degradation rates of acetaldehyde and toluene. In addition, the degradation efficiency of both acetaldehyde and toluene firstly increases, and stays at a relatively constant value, indicating the balance between the assumption and release of active sites. Despite the high K_{obs} of Fc-CHO/NU samples, especially Fc-CHO/NU-2 and Fc-CHO/

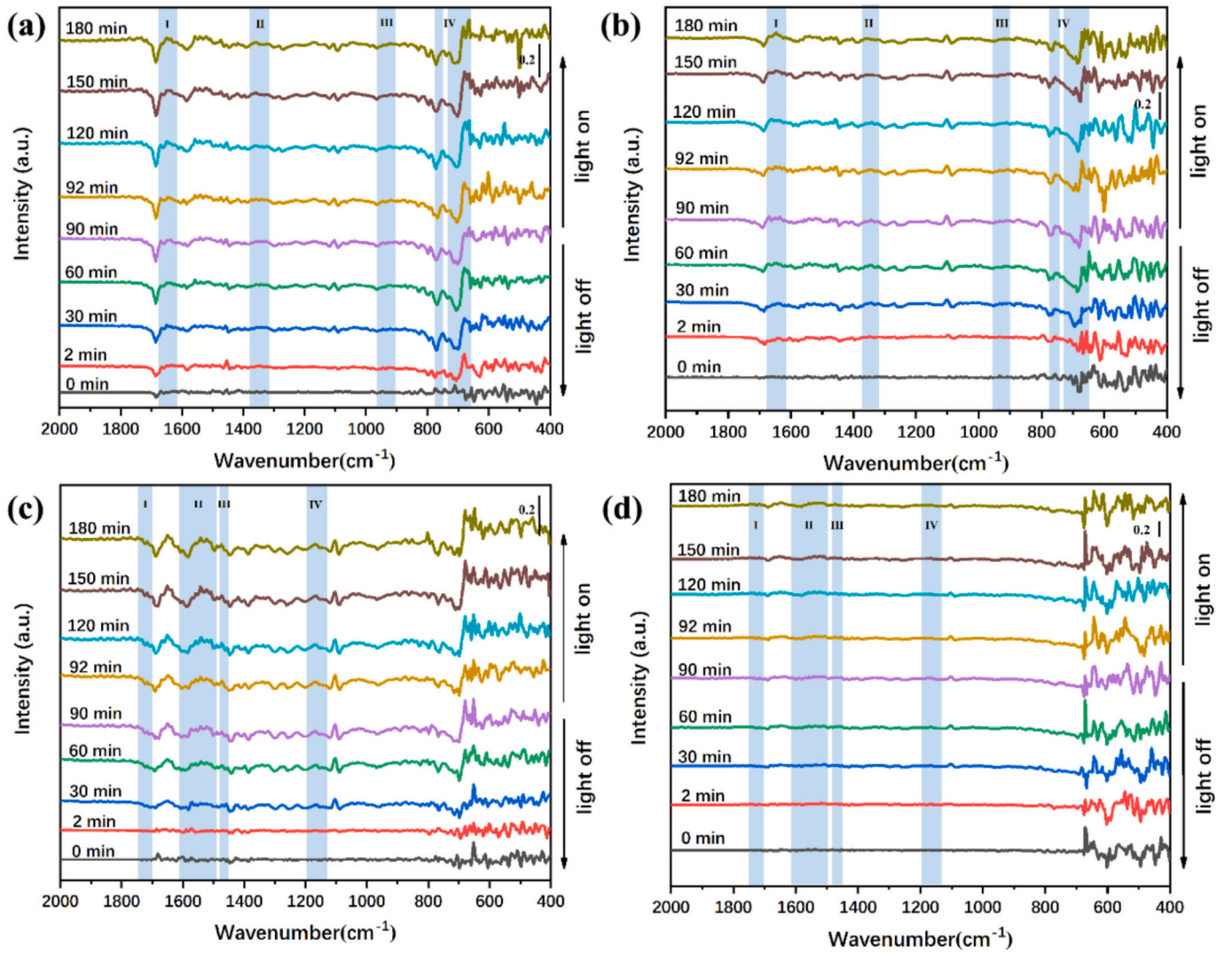

Fig. 6. The in-situ DRIFT spectra collected during the adsorption and photocatalytic degradation of (a) acetaldehyde on NU-0, (b) acetaldehyde on Fc-CHO-NU-2, (c) toluene on NU-0 and (d) toluene on Fc-CHO/NU-3 in the wavenumber range of 2000–400 cm^{-1}. The enlarged spectra could be found in the supplementary information (Figs. S6 to S9).

NU-3, they take longer time to achieve equilibrium, confirming their larger numbers of active sites for the adsorption of toluene.

Cyclic degradation experiments are also conducted for toluene and acetaldehyde to confirm the stability of Fc-CHO/NU. As given by Fig. S11, no obvious performance retention is observed, confirming the long-term stability of the Fc-CHO/NU photocatalysts. XRD patterns and ICP-OES results of Fc-CHO/NU photocatalysts before and after the cyclic reactions are collected (Table S1 and Fig. S12). The lattice structure and Fe ratio remain stable, indicating the high resistance to photo-corrosion and Fe-leaching of Fc-CHO/NU samples, which contributes to the stable degradation efficiency observed during the cyclic experiments and makes Fc-CHO/NU promising candidates for practical applications. To confirm the degradation of VOCs, the mineralization ratios of acetaldehyde and toluene are analyzed by monitoring the concentration of CO_2 in the outlet gas. As given by Fig. S13, the total mineralization ratios of toluene by Fc-CHO/NU-3 and acetaldehyde by Fc-CHO/NU-2 was calculated as 76.5 % and 80.7 %, respectively. The mineralization ratio of toluene experiences a decrease with the photocatalytic proceeds, and then gradually recovers to a steady value of ~78 %. This change could be attributed to the slow mineralization rate due to the complex structure of toluene, which results in a certain lag in the evolution of CO_2 concentration compared to the degradation efficiency. The mineralization ratio of acetaldehyde firstly reaches a value higher than 100 %, and gradually decrease to a steady value of ~62 %. The unreasonably high value might be originated from the fact that the photocatalytic reaction is at an unsteady state during the initial stage.

To further understand the degradation mechanisms of toluene and acetaldehyde, the mid-products formed during the adsorption and degradation of VOCs are monitored through in-situ FTIR and PTR-ToF-MS. Peaks for alcohols and carboxylic acid appeared in the in-situ FTIR spectra during the degradation of acetaldehyde (1320–1360 cm^{-1}, 650–771 cm^{-1}) (Fig. 6a), confirming their existence as intermediates. Similarly, methanol, ethanol and acetic acid are found as the dominant mid-products in the PTR-ToF-MS results (Fig. S13). Compared with NU, which shows a much stronger signal of alcohols, the formation of carboxylic acid is promoted in Fc-CHO/NU-2, which might be related to the higher concentration of •OH radicals.

Differences are also observed during the degradation of toluene by NU and Fc-CHO/NU samples (Fig. 6b and Fig. S14). Almost no new peak is observed during the photocatalytic degradation of toluene by pristine NU, except for an increase in the peaks assigned to benzyl species, indicating the accumulation of benzyl species, including benzene and benzaldehyde, on the surface of NU. When using Fc-CHO/NU-3 as the photocatalyst, new peaks for C—C bonds are found (1149–1192 cm^{-1}),

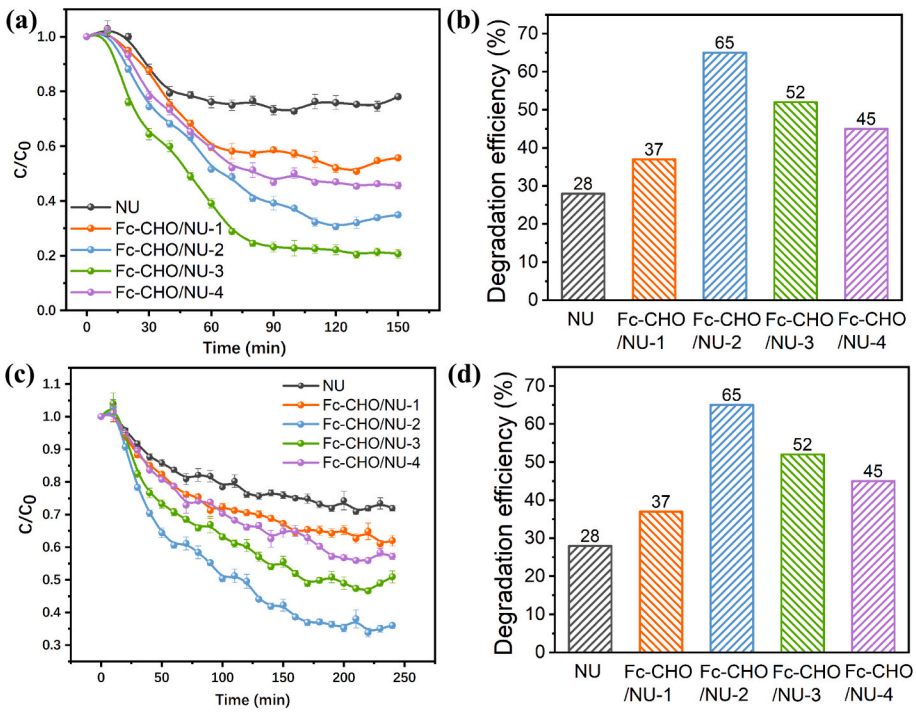

Fig. 7. (a) Degradation curves and (b) histograms of degradation efficiency for different samples towards 20 ppm toluene, and (c) degradation curves and (d) histograms of degradation efficiency towards 200 ppm acetaldehyde.

which could be attribute to the formation of small ring-opening molecules like methanol, ethanol, acetaldehyde, acetone and acetic acid, as detected through the PTR-ToF-MS. The direct charge transfer through π-π interaction and the formation of hydroxyl radicals might be the main reason for the deep oxidation and degradation of toluene.

Herein, the degradation mechanisms of acetaldehyde and toluene by Fc-CHO/NU photocatalysts are proposed. Fe-OH, Zr-OH and -NH_2 groups are found as the main active sites for acetaldehyde adsorption through hydrogen bonds. The generation of both $\bullet O_2^-$ and •OH radicals enable the oxidization of acetaldehyde into CO_2 and small molecules like methanol and acetic acid. Unlike the circumstance of pristine NU, in which ethanol was preferentially formed, the formation of abundant •OH radicals in Fc-CHO/NU-2 promote the transformation of absorbed acetaldehyde into acetic acid and then the complete mineralization. Humidity control experiment further confirms the key role of •OH radicals (Fig. S15a), with the absence of which the degradation efficiency dropped to only ~8 %. Similarly, due to the differences in the adsorption behavior of toluene on NU and Fc-CHO/NU, its degradation paths vary from the beginning. The degradation of toluene by NU starts from the oxidation of substituent -CH_3 groups by Zr nodes and $\bullet O_2^-$. Benzyl species like benzaldehyde are found as the dominant intermediates. Due to the lack of •OH radicals, the accumulation of benzyl species happens, which cover the active sites and explain the relatively low degradation efficiency and easy deactivation of NU. The grafting of Fc groups provides new π-π stacking sites for the adsorption of toluene. Direct charge transfer through π-π stacking lowers the energy barrier for the ring-opening of toluene, which, together with the effective generation of •OH radicals by Fc-CHO/NU-3, result in the high mineralization ratio and degradation efficiency of toluene. The role of •OH radical is also confirmed through humidity control experiments (Fig. S14b). Without the introduction of water, which is an important precursor for •OH radicals, a rapid deactivation of photocatalyst is observed, indicating that the ring-opening and mineralization of toluene cannot proceed successfully without the effective generation of •OH radicals.

3.5. Degradation of mixed toluene and acetaldehyde

Catalyst application scenarios often contain multiple VOCs. Adsorption and degradation studies of mixed VOCs by catalysts are more complex than single VOC. Herein, toluene and acetaldehyde, as co-exitance pollutants, are mixed to study their adsorption and degradation behavior. Fig. 8a and b shows the degradation efficiency of toluene and acetaldehyde by different samples. The presence of toluene results in a lower degradation efficiency of acetaldehyde by NU from 28 % to 8 %. On the contrary, the presence of acetaldehyde increases the degradation efficiency of toluene from 25 % to 84 %. The introduction of Fc-CHO reduces the degradation efficiency of NU for toluene in mixed VOCs from 84 % to 76 % and increases the degradation efficiency of NU for acetaldehyde from 8 % to 27 %. Comprehensively considering the concentration of toluene (10 ppm) and acetaldehyde (200 ppm), the introduction of Fc-CHO shows a positive effect for the purification of mixed pollutants.

In order to understand the differences between single and mixed systems, in-situ DRIFTs spectra were collected during the adsorption and photocatalytic degradation of acetaldehyde/toluene mixed gases (Fig. 8 c-e and Fig. S16). As given in Fig. 8 c, when using NU as the photocatalysts, the characteristic peaks for the adsorption of both acetaldehyde and toluene are found. However, unlike the circumstance of single acetaldehyde or toluene, the characteristic peaks of aldehyde groups (~1558 cm^{-1}) benzyl species (1600 and 1500 cm^{-1}) are weakened in the mixed system. The limited number of open active Zr-OH sites and the competitive adsorption between acetaldehyde and toluene might be the main reason. A strong peak at 1681 cm^{-1} appears, revealing the formation of unsaturated aldehydes. As reported by Dong et al., the co-adsorption of aldehydes and aromatic hydrocarbons would lead to hydrocarbon *ortho*-addition reactions [43], which results in the formation of 2-acetylbenzaldehyde in the acetaldehyde-toluene mixtures. The implantation of CH_3CO- substituent activates the benzene ring and promotes the ring-opening and deep mineralization of toluene. An increase in the removal efficiency of toluene is observed. However, the competitive adsorption between the two VOCs hinders the effective

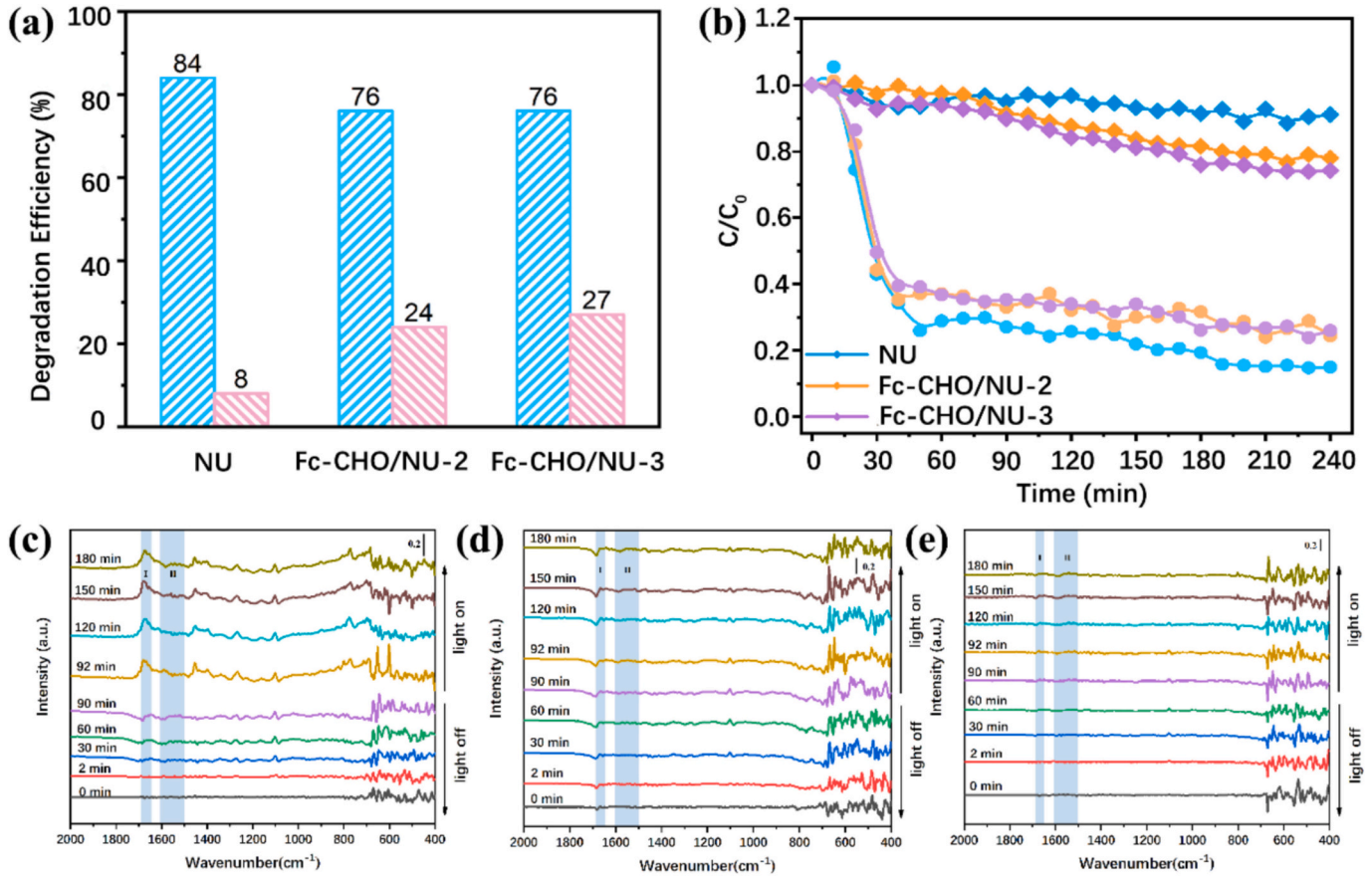

Fig. 8. (a) Degradation curves of different samples for mixed VOCs. (The circular icon represented toluene and the rhombic icon represented acetaldehyde); (b) The corresponding degradation efficiencies of different samples. (Blue for toluene, pink for acetaldehyde); The in-situ FTIR spectra collected during the adsorption and photocatalytic degradation of acetaldehyde/toluene mixed gases by (c) NU, (d) Fc-CHO/NU-2 and (e) Fc-CHO/NU-3 in the range of 2000–400 cm^{-1}. The enlarged in-situ FTIR spectra could be found in the supplementary information (Figs. S16 to S18).

capture of acetaldehyde, which therefore decrease its removal efficiency. In addition, the degradation of 2-acetylbenzaldehyde may generate acetaldehyde as an intermediate, which also accounts for the relatively lower removal efficiency of acetaldehyde. With the dosage of Fc-CHO, more active sites are introduced and the adsorption of both acetaldehyde and toluene are promoted. In addition, the FTIR curves become similar to the degradation of single toluene on Fc-CHO/NU-3 sample, confirming that the co-existence of acetaldehyde does not interfere with the ring-opening and mineralization of toluene through the π-π charge transfer paths.

Based on the above discussion, herein we propose the synergistic effects between charge transfer, adsorption and photocatalytic degradation of acetaldehyde and toluene in Fc-CHO/NU and the corresponding degradation mechanism (Scheme 1). When grafting Fc-CHO onto *reo*NH_2-UiO-66 through the Schiff-base reaction, electrons would soon migrate from Fc-CHO to NU, leading to the formation of Fe(III) and the increase in the electron density of Zr nodes. Despite the fact that Fc-CHO grafting sacrifices some of the -NH_2 as active sites, and weakens Zr as Lewis acid sites, the adsorption capacities of both toluene and acetaldehyde increase. π-π stacking and Fe-OH sites introduced by Fc-CHO alter the adsorption behavior and result in a significant increase in the adsorption capacity for the target molecules. The efficient enrichment of VOCs promotes their reaction with oxidative species on photocatalysts, which accelerates the degradation rate and improves the degradation efficiency. Under light illumination, Fc-CHO, with an off-domain electronic structure, promotes the separation of excited electron-hole pairs in NU and increases the proportion and migration of long-lifetimes carriers. The excited charge carriers migrate to the surface of the photocatalyst and accelerates the generation of oxidative $\cdot O_2^-$ radicals. In addition, the Fe(II)/Fe(III) transition under light illumination led to the formation of •OH, a key radical for photocatalytic oxidation. As a combined effect of the increased adsorption capacity, modified interface interactions and the effective generation of oxidative radicals, the degradation efficiency, degradation kinetics and mineralization ratio are all optimized in Fc-CHO/NU samples. For acetaldehyde, the oxidation reaction dominates in Fc-CHO/NU, resulting in the generation of carboxyl acids as the intermediates. Both $\cdot O_2^-$ and •OH radicals contribute to the effective degradation of acetaldehyde. For toluene, the direct electron transfer through π-π stacking, together with the generation of •OH radicals, enable the ring-opening and deep oxidation of toluene into CO_2 and H_2O. The complete degradation of adsorbed VOCs further releases active sites for the continuous adsorption to achieve an adsorption-degradation equilibrium, exhibiting the synergistic effects between adsorption and photocatalytic degradation. When further considering the circumstance of mixed pollutants, both competitive and synergistic effects are observed. On one hand, the competitive adsorption on Zr-OH sites shows adverse effect on the adsorption of both toluene and acetaldehyde. On the other hand, the catalytic addition reaction between acetaldehyde and toluene activates the benzene ring and promotes the ring-opening of benzyl species, which releases active sites for the further adsorption of VOCs.

4. Conclusion

In this work, *reo*-NH_2-UiO-66 (NU) containing cluster defects is modified by introducing different amounts of Fc-CHO. The Schiff-base

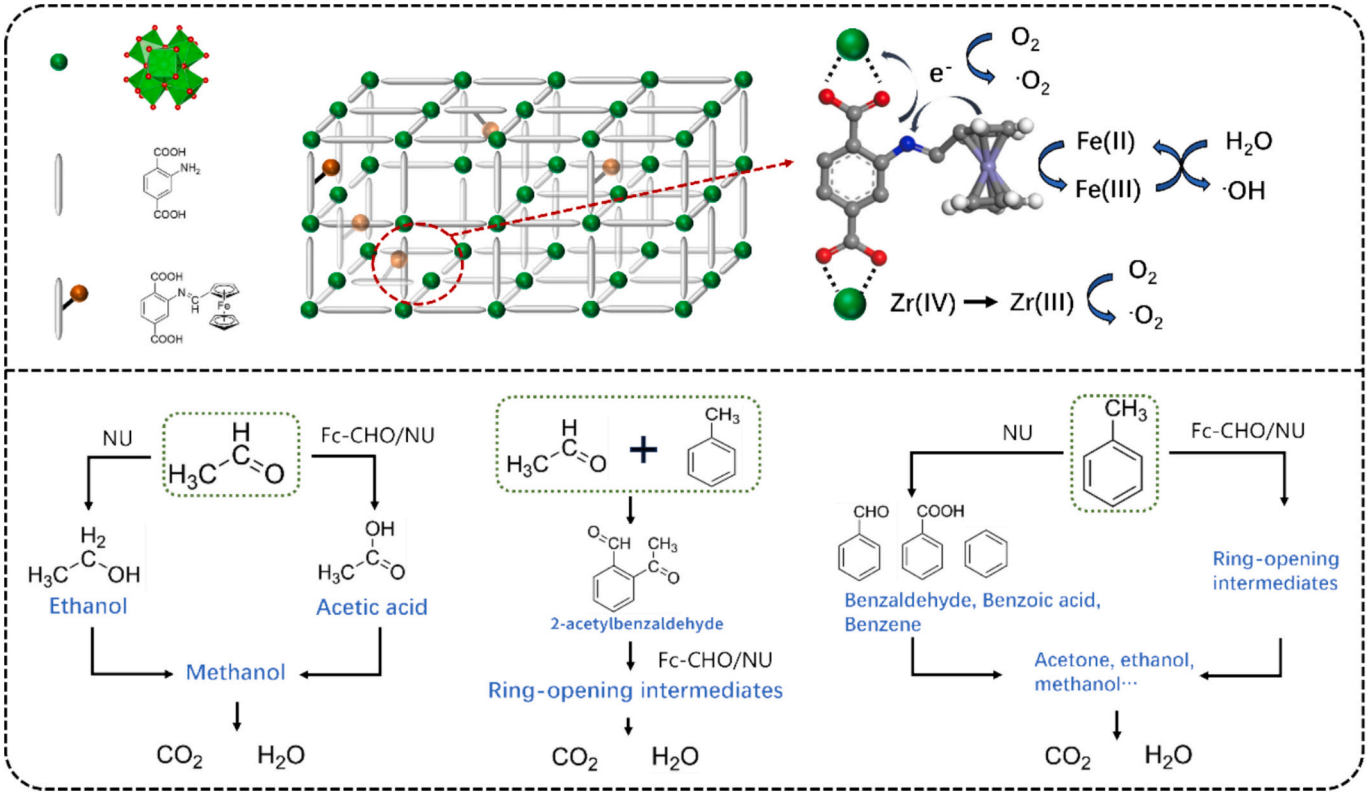

Scheme 1. The charge transfer between Fc-CHO and NU for the degradation of acetaldehyde and toluene.

reaction between Fc-CHO and -NH_2 preserve open Zr sites as active adsorption sites and provides new migration paths for charge carrier, which solves the dilemma of LMCT promotion and active sites sacrifice. As a consequence of the electron-donating and photosensitizing effects of Fc-CHO, both the light absorption and electron-hole separation in Fc-CHO/NU samples are optimized, which effectively promotes the generation of oxidative radicals for the degradation of VOCs. The dosage of Fc-CHO also influences the adsorption behavior of various VOCs by providing new Fe-OH sites for acetaldehyde and π-π interactions for toluene, which increases the adsorption capacity of acetaldehyde and toluene by nearly 2 times. The degradation efficiency of Fc-CHO/NU-3 for toluene was enhanced from 25 % (NU) to 80 %. The degradation efficiency of Fc-CHO/NU-2 for acetaldehyde was enhanced from 28 % (NU) to 65 %. In addition to single VOCs, the adsorption and degradation performance for acetaldehyde-toluene mixtures are also analyzed and both competitive and synergistic effects are observed. This work successfully addresses the critical challenge in MOFs photocatalysis by balancing the LMCT enhancement with the preservation of active sites. An effective bifunctional material for the enrichment and photocatalytic purification of VOCs is obtained. The superior adsorption properties of Fc-CHO/NU photocatalysts make them great candidates for the purification of trace VOCs (< 1 ppm) in indoor air. The photocatalytic catalytic degradation of VOCs with concentrations lower than 1 ppm will be carried out by applying pre-concentration detections in the future work to better meet the requirements of practical application. In addition, by selecting appropriate metallocene functional groups, the selective and efficient removal a broader-spectrum VOCs (like some chlorine or sulfur containing VOCs) could be expected, which opens up a new way for the design and fabrication of air purification materials.

CRediT authorship contribution statement

Jiajun Yu: Writing – original draft, Investigation, Data curation, Conceptualization. **Xiao Wang:** Writing – review & editing, Writing – original draft, Methodology, Investigation, Funding acquisition, Data curation, Conceptualization. **Shijie Yang:** Investigation, Data curation. **Xiaofeng Xie:** Writing – review & editing, Supervision. **Jing Sun:** Writing – review & editing, Supervision, Conceptualization.

Declaration of competing interest

The authors declare that they have no known competing financial interests or personal relationships that could have appeared to influence the work reported in this paper.

Acknowledgment

This work is supported by the Natural Science Foundation of Shanghai (22ZR1471800).

Appendix A. Supplementary data

Supplementary data to this article can be found online at https://doi.org/10.1016/j.cej.2025.166932.

Data availability

Data will be made available on request.

References

[1] K. Yang, L. Chen, X. Duan, G. Song, J. Sun, A. Chen, X. Xie, Ligand-controlled bimetallic Co/Fe MOF xerogels for CO_2 photocatalytic reduction, Ceram. Int. 49 (10) (2023) 16061–16069, https://doi.org/10.1016/j.ceramint.2023.01.204.
[2] J. Meng, X. Liu, C. Niu, Q. Pang, J. Li, F. Liu, Z. Liu, L. Mai, Advances in metal-organic framework coatings: versatile synthesis and broad applications, Chem. Soc. Rev. 49 (2020) 3142–3186, https://doi.org/10.1039/c9cs00806c.
[3] H. Zhang, S. Si, G. Zhai, Y. Li, Y. Liu, H. Cheng, Z. Wang, P. Wang, Z. Zheng, Y. Dai, et al., The long-distance charge transfer process in ferrocene-based MOFs with FeO6 clusters boosts photocatalytic CO_2 chemical fixation, Appl. Catal. B Environ. 337 (2023) 122909, https://doi.org/10.1016/j.apcatb.2023.122909.

[4] Q. Yang, Q. Xu, H.-L. Jiang, Metal–organic frameworks meet metal nanoparticles: synergistic effect for enhanced catalysis, Chem. Soc. Rev. 46 (15) (2017) 4774–4808, https://doi.org/10.1039/c6cs00724d.

[5] Z. Tang, H. Tao, X. Wang, L. Chen, C. Song, G. Lu, X. Xie, J. Sun, Quasi-in situ synthesis of Ag NPs@m-MIL-100(Fe) for the enhanced photocatalytic elimination of flowing xylenes, ACS Appl. Mater. Interfaces 14 (47) (2022) 52894–52906, https://doi.org/10.1021/acsami.2c15811.

[6] J. Yu, X. Wang, L. Chen, G. Lu, G. Shi, X. Xie, Y. Wang, J. Sun, Enhanced adsorption and visible-light photocatalytic degradation of toluene by CQDs/UiO-66 MOG with hierarchical pores, Chem. Eng. J. (2022) 435, https://doi.org/10.1016/j.cej.2022.135033.

[7] S. Yang, X. Wang, G. Song, G. Lu, G. Shi, Y. Wang, X. Xie, J. Sun, Ti-O-Mo bond-bridged PMA@MIL-125-NH_2 photocatalyst for gas acetone photocatalytic degradation, Applied Catalysis B: Environment and Energy 367 (2025) 115112, https://doi.org/10.1016/j.apcatb.2025.125112.

[8] S. Guo, C.W. Pan, M. Hou, Y.T. Hou, S. Yao, T.B. Lu, Z.M. Zhang, Dual regulation of sensitizers and cluster catalysts in metal-organic frameworks to boost H_2 evolution, Angew. Chem. Int. Ed. 64 (8) (2025) e202420398, https://doi.org/10.1002/anie.20242039.

[9] R. Li, J. Hu, M. Deng, H. Wang, X. Wang, Y. Hu, H.L. Jiang, J. Jiang, Q. Zhang, Y. Xie, et al., Integration of an inorganic semiconductor with a metal-organic framework: a platform for enhanced gaseous photocatalytic reactions, Adv. Mater. 26 (28) (2014) 4783–4788, https://doi.org/10.1002/adma.201400428.

[10] L. Chen, X. Wang, Z. Rao, Z. Tang, J.J.C.E.J. Sun, In-situ synthesis of Z-scheme MIL-100(Fe)/α-Fe_2O_3 heterojunction for enhanced adsorption and visible-light photocatalytic oxidation of o-xylene, Chem. Eng. J. 416 (6) (2021) 129112.

[11] Y. Kondo, S. Mizutani, Y. Kuwahara, K. Mori, T. Sekino, H. Yamashita, Perfluoroalkyl-functionalization of zirconium-based metal–organic framework nanosheets for photosynthesis of hydrogen peroxide from dioxygen and water, J. Mater. Chem. A 13 (5) (2025) 3701–3710, https://doi.org/10.1039/d4ta07808j.

[12] I. Ahmed, M.M.H. Mondol, M.J. Jung, G.H. Lee, S.H. Jhung, MOFs with bridging or terminal hydroxo ligands: applications in adsorption, catalysis, and functionalization, Coord. Chem. Rev. 475 (2023) 214912, https://doi.org/10.1016/j.ccr.2022.214912.

[13] S. Mandal, S. Natarajan, P. Mani, A. Pankajakshan, Post-synthetic modification of metal–organic frameworks toward applications, Adv. Funct. Mater. 31 (4) (2020) 2006291, https://doi.org/10.1002/adfm.202006291.

[14] S. Zhao, W. Huang, J. Xie, W. liu, Z. Qu, N. Yan, Mercury removal from flue gas using UiO-66-type metal-organic frameworks grafted with organic functionalities, Fuel 289 (2021) 119807, https://doi.org/10.1016/j.fuel.2020.119807.

[15] Y. Han, D. Brooks, M. He, Y. Chen, W. Huang, B. Tang, B. An, X. Han, M. Kippax-Jones, M.D. Frogley, et al., Enhanced benzene adsorption in chloro-functionalized metal-organic frameworks, J. Am. Chem. Soc. 146 (41) (2024) 28080–28087, https://doi.org/10.1021/jacs.4c0720.

[16] X. Zhao, C.-X. Tang, Q. Xu, H. Rao, D.-Y. Du, P. She, J.-S. Qin, Microenvironment modulation of Fe-porphyrinic metal–organic frameworks for CO_2 photoreduction, J. Catal. 439 (2024), https://doi.org/10.1016/j.jcat.2024.115745.

[17] J. Li, T. Musho, J. Bright, N. Wu, Functionalization of a metal-organic framework semiconductor for tuned band structure and catalytic activity, J. Electrochem. Soc. 166 (5) (2018) H3029–H3034, https://doi.org/10.1149/2.0051905jes.

[18] H. Werner, At least 60 years of ferrocene: the discovery and rediscovery of the sandwich complexes, Angew. Chem. Int. Ed. 51 (25) (2012) 6052–6058, https://doi.org/10.1002/anie.201201598.

[19] L. Xia, W. Zhou, Y. Xu, Z. Xia, X. Wang, Q. Yang, G. Xie, S. Chen, S. Gao, Ferrocene-boosting Zr-MOFs for efficient photocatalytic CO_2 reduction: a trade-off between enhancing LMCT and frustrating Lewis acid, Chem. Eng. J. 451 (2023), https://doi.org/10.1016/j.cej.2022.138747.

[20] C. Fang, Z. Deng, G. Cao, Q. Chu, Y. Wu, X. Li, X. Peng, G. Han, Co–ferrocene MOF/glucose oxidase as cascade nanozyme for effective tumor therapy, Adv. Funct. Mater. 30 (16) (2020), https://doi.org/10.1002/adfm.201910085.

[21] J. Liang, X. Gao, B. Guo, Y. Ding, J. Yan, Z. Guo, E.C.M. Tse, J. Liu, Ferrocene-based metal-organic framework nanosheets as a robust oxygen evolution catalyst, Angew. Chem. Int. Ed. 60 (23) (2021) 12770–12774, https://doi.org/10.1002/anie.202101878.

[22] Z. Xu, Y. Tao, Z. Sun, P. Bi, X. Zhong, J. Liao, D. Hao, L. Yang, L. Xu, M. Luo, et al., Ligand-engineered Ni-based metal–organic frameworks for electrochemical oxygen evolution reaction, Chem. Eng. J. 478 (2023), https://doi.org/10.1016/j.cej.2023.147418.

[23] Z. Huang, H. Yu, L. Wang, X. Liu, S. Ren, J. Liu, Ferrocene-modified UiO-66-NH_2 hybrids with g-C_3N_4 as enhanced photocatalysts for degradation of bisphenol A under visible light, J. Hazard. Mater. 436 (2022) 129052, https://doi.org/10.1016/j.jhazmat.2022.12905.

[24] Y. Yamaguchi, W. Ding, C.T. Sanderson, M.L. Borden, M.J. Morgan, C. Kutal, Electronic structure, spectroscopy, and photochemistry of group 8 metallocenes, Coord. Chem. Rev. 251 (3–4) (2007) 515–524, https://doi.org/10.1016/j.ccr.2006.02.028.

[25] J.E. Barnsley, S.O. Scottwell, A.B.S. Elliott, K.C. Gordon, J.D. Crowley, Structural, electronic, and computational studies of heteroleptic Cu(I) complexes of 6,6′-dimesityl-2,2′-bipyridine with ferrocene-appended ethynyl-2,2′-bipyridine ligands, Inorg. Chem. 55 (16) (2016) 8184–8192, https://doi.org/10.1021/acs.inorgchem.6b01300.

[26] W.-Y. Wang, N.-N. Ma, L. Wang, C.-L. Zhu, X.-Y. Fang, Y.-Q. Qiu, Effect of π-conjugate units on the ferrocene-based complexes: switchable second order nonlinear optics controlled by redox stimuli, Dyes Pigments 126 (2016) 29–37, https://doi.org/10.1016/j.dyepig.2015.11.006.

[27] B. Lan, J. Xu, L. Zhu, X. Chen, H. Kono, P. Wang, X. Zuo, J. Yan, A. Yagi, Y. Zheng, et al., Side-chain type ferrocene macrocycles, Precision Chemistry 2 (4) (2024) 143–150, https://doi.org/10.1021/prechem.3c00121.

[28] J. Yu, X. Wang, G. Lu, H. Xie, X. Xie, J. Sun, Improving the removal efficiency of oxygenated volatile organic compounds by defective UiO-66 regulated with water, J. Hazard. Mater. 469 (2024) 134055, https://doi.org/10.1016/j.jhazmat.2024.134055.

[29] Z. Xu, Y. Tao, Z. Sun, P. Bi, X. Zhong, J. Liao, D. Hao, L. Yang, L. Xu, M. Luo, et al., Ligand-engineered Ni-based metal-organic frameworks for electrochemical oxygen evolution reaction, Chem. Eng. J. 478 (2023) 147418, https://doi.org/10.1016/j.cej.2023.147418.

[30] S. Tatay, S. Martinez-Gimenez, A. Rubio-Gaspar, E. Gomez-Oliveira, J. Castells-Gil, Z. Dong, A. Mayoral, N. Almora-Barrios, M.P. N, C. Marti-Gastaldo, Synthetic control of correlated disorder in UiO-66 frameworks, Nat. Commun. 14 (1) (2023) 6962, https://doi.org/10.1038/s41467-023-41936-w.

[31] X. Feng, H.S. Jena, C. Krishnaraj, D. Arenas-Esteban, K. Leus, G. Wang, J. Sun, M. Ruscher, J. Timoshenko, B. Roldan Cuenya, et al., Creation of exclusive artificial cluster defects by selective metal removal in the (Zn, Zr) mixed-metal UiO-66, J. Am. Chem. Soc. 143 (51) (2021) 21511–21518, https://doi.org/10.1021/jacs.1c05357.

[32] Z. Huang, H. Yu, L. Wang, X. Liu, S. Ren, J. Liu, Ferrocene-modified UiO-66-NH_2 hybrids with g-C_3N_4 as enhanced photocatalysts for degradation of bisphenol A under visible light, J. Hazard. Mater. 436 (2022) 129052, https://doi.org/10.1016/j.jhazmat.2022.129052.

[33] C. Fang, Z. Deng, G. Cao, Q. Chu, Y. Wu, X. Li, X. Peng, G. Han, Co-ferrocene MOF/glucose oxidase as cascade nanozyme for effective tumor therapy, Adv. Funct. Mater. 30 (16) (2020) 1910085, https://doi.org/10.1002/adfm.201910085.

[34] Z. Li, B. Li, X. Wu, S.A. Sheppard, S. Zhang, D. Gao, N.J. Long, Z. Zhu, Organometallic-functionalized interfaces for highly efficient inverted perovskite solar cells, Science 376 (6591) (2022) 416, https://doi.org/10.1126/science.abm8566.

[35] J. Liang, X. Gao, B. Guo, Y. Ding, J. Yan, Z. Guo, E.C.M. Tse, J. Liu, Ferrocene-based metal-organic framework nanosheets as a robust oxygen evolution catalyst, Angew. Chem. Int. Ed. 60 (23) (2021) 12770–12774, https://doi.org/10.1002/anie.202101878.

[36] A. Zhou, C. Zhao, Y. Dou, Y. Zhang, Y. Jia, H. Ou, Z. Zhuang, Y. Xie, W. Zhang, D. Wang, et al., Extension of charge separation distance over isolated dual-metal sites in metal-organic frameworks for efficient CO_2 photoreduction, Applied Catalysis B: Environment and Energy (2025) 372, https://doi.org/10.1016/j.apcatb.2025.125297.

[37] N. Kolobov, M.G. Goesten, J. Gascon, Metal-organic frameworks: molecules or semiconductors in photocatalysis? Angew. Chem. Int. Ed. 60 (50) (2021) 26038–26052, https://doi.org/10.1002/anie.202106342.

[38] E. Barea, C. Montoro, J.A.R. Navarro, Toxic gas removal – metal–organic frameworks for the capture and degradation of toxic gases and vapours, Chem. Soc. Rev. 43 (16) (2014) 5419–5430, https://doi.org/10.1039/C3CS60475F.

[39] P. Ji, X. Feng, P. Oliveres, Z. Li, A. Murakami, C. Wang, W. Lin, Strongly Lewis acidic metal-organic frameworks for continuous flow catalysis, J. Am. Chem. Soc. 141 (37) (2019) 14878–14888, https://doi.org/10.1021/jacs.9b07891.

[40] P. Ji, T. Drake, A. Murakarni, P. Oliveres, J.H. Skone, W. Lin, Tuning Lewis acidity of metal-organic frameworks via perfluorination of bridging ligands: spectroscopic, theoretical, and catalytic studies, J. Am. Chem. Soc. 140 (33) (2018) 10553–10561, https://doi.org/10.1021/jacs.8b05765.

[41] R. Li, J. Hu, M. Deng, H. Wang, X. Wang, Y. Hu, H.-L. Jiang, J. Jiang, Q. Zhang, Y. Xie, et al., Integration of an inorganic semiconductor with a metal-organic framework: a platform for enhanced gaseous photocatalytic reactions, Adv. Mater. 26 (28) (2014) 4783, https://doi.org/10.1002/adma.201400428.

[42] L. Chen, X. Wang, Z. Rao, Z. Tang, G. Shi, Y. Wang, G. Lu, X. Xie, D. Chen, J. Sun, One-pot synthesis of the MIL-100 (Fe) MOF/MOX homojunctions with tunable hierarchical pores for the photocatalytic removal of BTXS, Appl. Catal. B Environ. (2022) 303, https://doi.org/10.1016/j.apcatb.2021.120885.

[43] J. Li, R. Chen, W. Cui, X.A. Dong, H. Wang, K.-H. Kim, Y. Chu, J. Sheng, Y. Sun, F. Dong, Synergistic photocatalytic decomposition of a volatile organic compound mixture: high efficiency, reaction mechanism, and long-term stability, ACS Catal. 10 (13) (2020) 7230–7239, https://doi.org/10.1021/acscatal.0c00693.